Prepared for submission to JCAP

The Impact of Spectroscopic Redshift Errors on Cosmological Measurements

Shengyu He,[a] **Jiaxi Yu**,[a,b] **Antoine Rocher**,[a] **Daniel Forero-Sánchez**,[a,c] **Jean-Paul Kneib**,[a] **Cheng Zhao**,[d] **Etienne Burtin**,[e] **Jiamin Hou**[f,g]

[a]Institute of Physics, Laboratory of Astrophysics, École Polytechnique Fédérale de Lausanne (EPFL), Observatoire de Sauverny, CH-1290 Versoix, Switzerland

[b]Kavli Institute for the Physics and Mathematics of the Universe (WPI), The University of Tokyo Institutes for Advanced Study (UTIAS), The University of Tokyo, Chiba 277-8583, Japan

[c]Institut de Ciències del Cosmos (ICCUB), Universitat de Barcelona (UB), c. Martí i Franquès, 1, 08028 Barcelona, Spain.

[d]Department of Astronomy, Tsinghua University, Beijing 100084, China

[e]IRFU, CEA, Université Paris-Saclay, F-91191 Gif-sur-Yvette, France

[f]Institute of Astronomy, University of Cambridge, Madingley Rd, Cambridge CB3 0HA, UK

[g]Kavli Institute for Cosmology Cambridge, Madingley Road, Cambridge CB3 0HA, UK

E-mail: shengyu.he@epfl.ch, jiaxi.yu@ipmu.jp, antoine.rocher@epfl.ch

Abstract. Spectroscopic redshift errors, including redshift uncertainty and catastrophic failures, can bias cosmological measurements from galaxy clustering at sub-percent level. In this work, we investigate their impact on the full-shape analysis using contaminated mock catalogs. We find that redshift uncertainty introduces a scale-dependent damping effect on the power spectrum, which is absorbed by counterterms in clustering model, keeping parameter biases below 5%. Catastrophic failures suppress the power spectrum amplitude by an approximately constant factor, which scales with the catastrophic rate f_c. While this effect is negligible for DESI galaxy populations ($f_c = 1\%$), the slitless-like errors, combining redshift uncertainty with $f_c = 5\%$ catastrophics, introduce significant biases in cosmological constraints. In this case, we find 6% to 16% shifts ($\sim 2.2\sigma$ level) in estimating the fractional growth rate $df \equiv f/f^{\rm fid}$ and the log primordial amplitude $\ln(10^{10}A_s)$. Applying the correction factor $(1-f_c)^2$ on the galaxy power spectrum mitigates the bias but weakens the parameter constraints due to new degeneracies. Alternatively, fixing f_c to its expected value restores the constraining power with a modest bias of 1.0σ. Our results indicate that for space-based slitless surveys such as *Euclid*, at minimum accurate estimation of f_c and its incorporation into the clustering model are necessary to get unbiased cosmological inference. Extending to evolving dark energy and massive neutrino cosmologies, redshift errors do not bias the dark energy properties parametrized by w_0 and w_a, but can degrade constraints on the summed neutrino mass $\sum m_\nu$ by up to 80% in the worst case.

arXiv:2508.21182v4 [astro-ph.CO] 16 Dec 2025

Contents

1 Introduction **2**

2 Spectroscopic Survey and Redshift Errors **3**
- 2.1 Redshift uncertainty 3
- 2.2 Redshift catastrophic failures 4
- 2.3 Combined errors for Slitless redshift surveys 5

3 Contaminated Mocks **5**

4 Methods **7**
- 4.1 Power spectrum estimator 7
- 4.2 Galaxy clustering models 7
  - 4.2.1 Effective-field theory of LSS 7
  - 4.2.2 Full-Shape fitting approaches 8
- 4.3 Clustering effect of redshift errors 9
  - 4.3.1 Redshift uncertainty damping 9
  - 4.3.2 Redshift catastrophics correction 10
- 4.4 Cosmological inference and Covariance matrices 10

5 Results **11**
- 5.1 Impact of redshift errors on clustering statistics 11
- 5.2 Baseline Fitting 12
  - 5.2.1 Cosmological influence 12
  - 5.2.2 Catastrophics-correction for slitless survey 15
- 5.3 Beyond ΛCDM cosmologies 17
  - 5.3.1 Evolving dark energy 17
  - 5.3.2 Massive neutrinos 18

6 Conclusions **18**

A BAO fitting results **24**

B χ^2 results for baseline analysis **25**

1 Introduction

The large-scale structure (LSS) observed by galaxy redshift surveys has played an important role in advancing our understanding of fundamental physics. Clustering features, such as baryon acoustic oscillations (BAO; [1–5]), and the full-shape power spectrum [6–9], have been used to constrain some key quantities in cosmology, including dark energy equation of state w, the matter density $\Omega_{\rm m}$, the structure growth rate $f\sigma_8$, neutrino mass $\sum m_\nu$ and possible deviations from general relativity. Current leading experiments, the Dark Energy Spectroscopic Instrument[1] (DESI; [10, 11]), and the ongoing space mission *Euclid*[2] [12, 13] are mapping the three-dimensional Universe by measuring redshifts for tens to hundreds of millions galaxies. These surveys will cover over more than 15,000 deg^2 of the sky, and trace the LSS back to redshift ~ 3.5. This large probing volume allows the clustering signal to be measured with minimal cosmic variance, leading to sub-percent precision in cosmological measurements. Given this level of precision, detailed studies on systematic errors are critical to ensure the robustness and reliability of cosmological constraints.

Among various observational systematics, we focus on the impact of spectroscopic redshift errors. They persist in data with secure redshifts, where redshift calibration and algorithmic processing have already been applied [14–17]. There are two primary types of errors: redshift uncertainty and redshift catastrophic failures. Redshift uncertainty refers to minor shifts ($\Delta z \sim 10^{-4}$) in all redshift measurements, primarily caused by instrumental noise and the intrinsic width of spectral features. In contrast, redshift catastrophic failures result from the misidentification of spectral lines, leading to severely incorrect redshifts ($\Delta z \sim 10^{-2}$) in a small fraction of data. These systematic errors can distort the observed clustering signal and potentially bias the cosmological inference. While previous studies have examined their individual impacts [18–23], a comprehensive analysis that considers all these effects remains unexplored. This work aims to bridge that gap and explore their combined influence on cosmological inference from full-shape clustering analysis.

The spectroscopic redshift errors can be quantified using repeated redshift observations and incorporated into realistic galaxy mocks (e.g., [21, 24–26]). By comparing analyses on clean mocks with those contaminated by redshift errors, we can assess their impact on clustering statistics and cosmological constraints. Improved facilities and increased statistics in DESI [21, 27] provide a better way to model the redshift errors and study their impact on cosmological analyses. Additionally, space-based surveys such as *Euclid* use slitless spectroscopy at near-infrared to measure redshifts [28, 29]. This method requires no pre-selection of targets and is particularly effective for probing high-redshift galaxies. However, it is also more susceptible to redshift errors due to the lower spectrum resolution and the potential overlap of different spectra. These challenges have been addressed in the context of redshift interlopers for *Euclid* [23]. In this work, we use hypothetical combined redshift errors to represent the conditions expected in slitless surveys. This approach provides a description of the related systematics and offers practical guidance for interpreting and mitigating their impact in cosmological analyzes for spectroscopic surveys.

The outline of the paper is as follows: section 2 introduces two galaxy redshift surveys, DESI and *Euclid*, and the spectroscopic redshift errors. section 3 describes how we construct our contaminated mock catalogs. section 4 presents the methodologies used to derive cosmological inferences from the mock data. In section 5, we present the impact of redshift errors

[1] DESI, desi.lbl.gov
[2] *Euclid*, cosmos.esa.int/web/euclid

on clustering statistics and how these propagate into the cosmological parameter constraints, including extensions w_0w_aCDM and massive neutrino. Finally, we summarize our findings and conclude in section 6.

2 Spectroscopic Survey and Redshift Errors

Spectroscopic surveys measure the redshifts of objects with high precision by analyzing their spectral features, such as emission and absorption lines. Two massive ongoing spectroscopic surveys, DESI and *Euclid*, are measuring galaxy clustering with unprecedented accuracy. In its first three years, the ground-based survey DESI has observed over 14 million galaxies [5] and plans to extend its initial plan to 60M galaxies across 18,000 $\deg^2$. Its dark matter tracers include Bright Galaxies (BGS) at $0.1 < z < 0.4$ [30], Luminous Red Galaxies (LRG) at $0.4 < z < 1.1$ [31], Emission Line Galaxies (ELG, mainly [O II] emitters) at $0.6 < z < 1.6$ [32], and Quasi-Stellar Objects (QSO) at $0.8 < z < 3.5$ [33]. In parallel, the *Euclid* mission is conducting slitless spectroscopic survey from space and aim to observe tens of millions of galaxies over 15,000 $\deg^2$. Its primary targets are [H α] emitters in the redshift range $0.9 < z < 1.8$ [13]. The *Euclid* Quick Data Release 1 (QR1) is already publicly available [34]. The large cosmic volumes probed by DESI and *Euclid* enable sub-percent precision in cosmological measurements and require a rigorous understanding of systematic errors, particularly those related to redshift measurements.

In this work, the spectroscopic systematic redshift errors are referred to as *redshift errors*. The redshift errors exist in both ground-based and space-based galaxy redshift surveys. These include redshift uncertainty, the small statistical fluctuations in redshift measurements, and redshift catastrophic failures, the large errors from the true values. Both types of error exists in secure redshift measurements, i.e., those that have been calibrated and successfully passed the redshift determination pipeline. Consequently, these hidden errors can distort the observed clustering pattern and potentially bias our cosmological analyses. Since both redshift uncertainty and catastrophic failures can be quantified from repeated redshift observations, e.g. $dv_{ij} = c(z_i - z_j)/(1 + z_i)$, it is practical to analyze them together. This combined treatment is also relevant for space missions such as *Euclid*, which apply slitless spectroscopy to measure redshifts and are more susceptible to both types of contamination. In the following, we will describe how redshift uncertainty and redshift catastrophic failures are characterized and modeled, and what are the redshift errors expected in slitless spectroscopic surveys.

2.1 Redshift uncertainty

Redshift uncertainty is an inevitable systematic error in spectroscopic redshift measurements. It arises because the spectral lines used to determine redshifts have specific widths rather than being ideal delta functions. These widths can result from a combination of physical (e.g., galaxy thermal motions, turbulence, gravitational broadening) and observational (e.g, instrumental resolution, observing condition) effects. The values of redshift uncertainty are reported for different types of targets within different redshift surveys. For example, in eBOSS galaxy samples, the redshift accuracies, characterized by the root mean square (RMS) of dv_{ij}, are about 65.6, 20 and 300 $\mathrm{km \cdot s^{-1}}$ for LRG, ELG and QSO [35–37]. From DESI Visual Inspection, the redshift precisions, defined as the median absolute deviation (MAD) values of dv_{ij}, reaches about 10, 10, 40 and 100 $\mathrm{km \cdot s^{-1}}$ for BGS, ELG, LRG and QSO respectively [38, 39].

The effect of redshift uncertainty is equivalent to randomly smearing the peculiar velocity of an observed object along the line-of-sight. This smearing velocity, $\Delta v_{\rm smear}$, defined as the same as dv_{ij}, is empirically quantified using redshift difference. The distribution of observed $\Delta v_{\rm smear}$ can be statistically modeled. For galaxies, this distribution is typically Gaussian $\mathcal{N}(\mu,\, \sigma_{\Delta v})$, with $\sigma_{\Delta v}$ characterizing the redshift uncertainty dispersion [25, 26, 35]:

$$\mathcal{N}(\Delta v_{\rm smear}\,|\,\mu,\, \sigma_{\Delta v}) = \frac{1}{\sqrt{2\pi}\sigma_{\Delta v}} \exp\left(-\frac{(\Delta v_{\rm smear}-\mu)^2}{2\sigma_{\Delta v}}\right) \tag{2.1}$$

For QSO, the distribution of $\Delta v_{\rm smear}$ usually exhibits extended wide tails. In such case, a multiple-Gaussian model [33, 37] or a Lorentzian distribution [26] provide a better fit to repeat observations. In our work, we use the Lorentzian profile, $\mathcal{L}(\,p,\, {\rm w}_{\Delta v})$, to describe the QSO redshift uncertainty with extended tail:

$$\mathcal{L}(\Delta v_{\rm smear}\,|\,p,\, {\rm w}_{\Delta v}) = \frac{1}{1+((\Delta v_{\rm smear}-p)/{\rm w}_{\Delta v})^2} \tag{2.2}$$

Here, ${\rm w}_{\Delta v}$ captures the width of the distribution, thus characterizing the redshift uncertainty in the Lorentzian profile. To assess how the presence of long-tailed uncertainty distributions may impact clustering and cosmological measurements, we adopt both Gaussian and Lorentzian profiles to model QSO redshift uncertainty. A comparison between these profiles is shown in the left panel of Figure 1.

2.2 Redshift catastrophic failures

Redshift catastrophic failures (or redshift catastrophics) arise in a small fraction of redshift measurements, typically identified through significant redshift differences in repeated observations. These errors can result from misidentification of sky residuals or confusion between spectral lines of different galaxies [14, 17, 21]. Faint or ambiguous spectral features can also lead to catastrophically incorrect redshifts. The catastrophic contamination rate, f_c, and the threshold for identifying it vary in different surveys. For example, the WiggleZ survey reports 5% f_c of redshift blunders with $|\Delta z| > 400\,{\rm km\cdot s^{-1}}$ (larger than $4\sigma_{\Delta v}$) [14]. In eBOSS, the reported f_c is less than 1% for LRGs and ELGs ($|\Delta z| > 1000\,{\rm km\cdot s^{-1}}$) and 1.6% for quasars ($|\Delta z| > 3000\,{\rm km\cdot s^{-1}}$) [35–37]. For DESI DR1, using the same $|\Delta z|$ thresholds as in eBOSS, the f_c is estimated to be less than 1% for all tracers at $z < 2.1$ [27].

In the study of DESI DR1 repeated ELG observations, redshift catastrophics are classified into two main categories: sky confusion at $z = 1.32$ and random catastrophics [21]. Sky confusion, responsible for 24% of these errors, arises from misidentifying residuals of sky emissions at around 8625 Å and can be approximated as a Gaussian distribution centered at the corresponding sky line positions. The remaining 76% are random catastrophic failures that encompass various error patterns. These can be modeled using a log-normal profile defined as follows:

$$\mathcal{LN}(\Delta\hat{v}_{\rm c}|\,\mu_{\rm ran}, \sigma^2_{\rm ran}, \hat{v}_0) = \frac{1}{\sqrt{2\pi}\sigma_{\rm ran}(-\Delta\hat{v}_{\rm c}+\hat{v}_0)} \exp\left\{-\frac{[\ln(-\Delta\hat{v}_{\rm c}+\hat{v}_0)-\mu_{\rm ran}]^2}{2\sigma^2_{\rm ran}}\right\} \tag{2.3}$$

This function models the absolute log-normal distribution of redshift catastrophics ($\Delta\hat{v}_{\rm c} = \log_{10}(|dv_{ij}|)$) with parameters $\mu_{\rm ran}$, $\sigma^2_{\rm ran}$ and $\hat{v}_0$. In our study, we focus on the random pattern while varying the contamination rate f_c to generalize catastrophic patterns for different surveys. We note that including sky confusion would not affect significantly the results [21]. The distributions of catastrophics for $f_c = 1\%$ and 5% are shown in the right panel of Figure 1, with the magnitude of $\Delta v_{\rm c}$ varying in 10^3–$10^6\,{\rm km\cdot s^{-1}}$.

2.3 Combined errors for Slitless redshift surveys

Space missions such as *Euclid* [13], Roman [40] and CSST (scheduled for launch in 2027; [41]) employ slitless spectroscopy to map the 3D distribution of galaxies over wide areas of sky. Early dataset from *Euclid* QR1 is now publicly available [34] and provides initial evaluations of the performance of space spectroscopic redshift measurement. Unlike traditional ground slit-based spectroscopy that use fibers to capture individual targets, slitless spectroscopy disperses the light from all sources in the field simultaneously, enabling efficient and continuous observations without the need for target pre-selection. This approach allows for high sky coverage and dense sampling of galaxies in the redshift range relevant to LSS studies.

However, the slitless design magnifies the redshift errors. *Euclid* spectroscopic redshifts are derived from spectra provided by the Near Infrared Spectro-Photometer (NISP; [28]), which operates with a resolution of $R \simeq 500$ [29]. In comparison, the ground-based DESI survey uses instruments with resolution $R \sim 2000$ to 5500 [10]. The lower spectral resolution and slitless spectroscopy pipeline lead to broader spectral lines and consequently increased redshift uncertainty. Additionally, the lack of spatial isolation between sources causes catastrophic redshift errors [17, 29], typically through cross-contamination and self-contamination. Cross-contamination arises from overlapping spectrograms of neighboring sources, while self-contamination results from the degeneracy between spatial and spectral information along the dispersion direction. These combined effects lead to a higher rate of redshift catastrophic failures in the sample [23].

To address these challenges, we adopt a hypothetical redshift error that combines both redshift uncertainty and catastrophics to simulate the expected observational systematics in slitless surveys. This model assumes a larger uncertainty than those typical of ELG (i.e., LRG-like, $\sigma_{\Delta v} = 85.7\,\mathrm{km}\cdot\mathrm{s}^{-1}$) and a higher rate of catastrophic failures ($f_c = 5\%$ with $|\Delta v| > 1000\,\mathrm{km}\cdot\mathrm{s}^{-1}$). For reference, [17] reports that the scatter of redshift difference between *Euclid* and DESI is $\sigma_{dz} = 0.8 \times 10^{-3} \approx 240\,\mathrm{km/s}$, and the overall success rate indicates that a catastrophic rate $f_c \gtrsim 10\%$ is expected. Therefore, our hypothetical scenario remains relatively optimistic compared to the current expectations from slitless survey.

3 Contaminated Mocks

We use the Quijote N-body simulation suite to construct our mock catalogs [42]. The Quijote fiducial simulations assume a flat ΛCDM universe, with cosmology consistent with the *Planck* 2018 result [43]: $h = 0.6711$, $\Omega_\mathrm{m} = 0.3175$, $\Omega_\mathrm{b} = 0.049$, $\sigma_8 = 0.834$, $n_s = 0.9624$, $\sum m_\nu = 0.0\,\mathrm{eV}$, $w = -1$. To study the impact of redshift errors on neutrino mass measurement, we also include the '*Mnu_p*' catalog with $\sum m_\nu = 0.1\,\mathrm{eV}$. In Quijote simulation, each realization contains 512^3 CDM particles with mass $m_p \approx 6.5 \times 10^{11}\,M_\odot$, evolved within a comoving box of volume $1\,h^{-3}\mathrm{Gpc}^3$. To match the redshift range of interest, we use the snapshots at redshift $z = 1.0$. A mass selection with $13.1 < \log_{10}(M_h/(h^{-1}M_\odot)) < 13.5$ is applied to ensure that the truncated halos represent the dominant structures contributing to the galaxy clustering. We use 500 realizations from the Quijote suite to construct mock catalogs contaminated by different types of redshift errors.

The halo catalogs include information such as the Cartesian positions X, Y, Z, the corresponding peculiar velocities $\boldsymbol{v}_\mathrm{pec}$, and the halo masses, M_h. Assuming the line-of-sight is along the x-direction, we use the x-component of the peculiar velocity, $v_{\mathrm{pec},x}$, to transform halo positions from real space to redshift space at redshift z: $X_\mathrm{rsd} = X_\mathrm{real} + v_{\mathrm{pec},x}\,(1+z)/H(z)$. The clean mock catalogs are built using this peculiar velocity without modification. To build

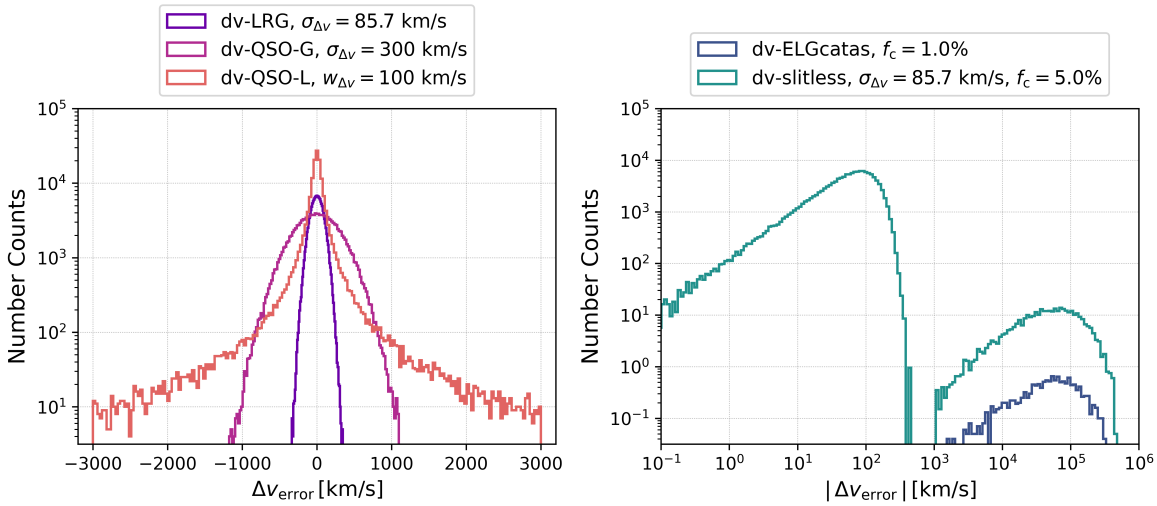

Figure 1: Comparisons of redshift error ($\Delta v_{\rm error}$) distributions. *Left*: Typical LRG-like and QSO-like redshift uncertainties, modeled by Gaussian smearing with $\sigma_{\Delta v}$ or Lorentzian smearing with $\mathrm{w}_{\Delta v}$. *Right*: ELG-like catastrophics with $f_c = 1\%$ and hypothetical slitless-like errors with LRG-like redshift uncertainty (left part) and $f_c = 5\%$ catastrophics (right part). These distributions are used to generate the velocity dispersion caused by redshift errors.

Mocks label	clean	dv-LRG	dv-QSO-G	dv-QSO-L	dv-ELGcatas	dv-slitless
$\sigma_{\Delta v}/\mathrm{w}_{\Delta v}$ ($\mathrm{km \cdot s^{-1}}$)	-	85.7	300	100	-	85.7
f_c	-	-	-	-	1%	5%

Table 1: Summary of contaminations and mock catalogs used in our study. Mocks include uncontaminated (clean) and those affected by redshift errors. We consider redshift uncertainties for LRG-like Gaussian (dv-LRG), QSO-like Gaussian (dv-QSO-G) and QSO-like Lorentzian (dv-QSO-L) profiles. Redshift catastrophic failures are based on analyses of DESI DR1 ELG repeat observations [21], with f_c being the contamination rate. We consider $f_c = 1\%$ with ELG-like catastrophic pattern (dv-ELGcatas) in DESI survey. For slitless-like errors (dv-slitless), we assume combined errors with LRG-like uncertainty and $f_c = 5\%$ ELG-like catastrophics to mimic the expected observing conditions in slitless survey like *Euclid*. The corresponding redshift error distributions applied in contaminated mocks are shown in Figure 1.

contaminated mocks with redshift errors, we add an additional velocity shift $\Delta v_{\rm error}$ to $v_{{\rm pec},x}$. This $\Delta v_{\rm error}$ simulates the line-of-sight velocity dispersion introduced by redshift errors.

To generate the $\Delta v_{\rm error}$ distribution, we use different profiles to simulate redshift errors for different surveys. For redshift uncertainty, we use the magnitudes reported from eBOSS and DESI Early Data Release (EDR) [19, 26]. Specifically, we apply Gaussian profiles in Eq. (2.1) with $\sigma_{\Delta v} = 85.7\,\mathrm{km \cdot s^{-1}}$ to simulate LRG-like smearing and $\sigma_{\Delta v} = 300\,\mathrm{km \cdot s^{-1}}$ for QSO-like smearing. We also consider a Lorentzian profile in Eq. (2.2) to mimic the extended tails observed in QSO redshift uncertainty. The Lorentzian profile is parametrized with $\mathrm{w}_{\Delta v} = 100\,\mathrm{km \cdot s^{-1}}$ and truncated by $\Delta v_{\rm smear} < 3000\,\mathrm{km \cdot s^{-1}}$. Using these values, we have almost the same RMS of $\Delta v_{\rm smear}$ for the QSO Gaussian and Lorentzian smearing. The

redshift smearing effects for ELG are small ($\sigma_{\Delta v} \sim 10\,\mathrm{km}\cdot\mathrm{s}^{-1}$; [21]) and we neglect them in this study. A summary of the configurations for the contaminated mocks is in Table 1, with the comparison of distributions shown in the left panel of Figure 1. In all cases, we assume the redshift errors are symmetric to zero (i.e., $\mu = 0$ and $p = 0$).

For redshift catastrophics, we adopt a model based on DESI DR1 ELG repeat observations [21]. The velocity shifts caused by catastrophics follow a symmetric distribution centered at zero, with each half modeled by the profile $\mathcal{LN}(\Delta\hat{v}_c\,|\,0.64, 0.25^2, 6.62)$ defined in Eq. (2.3). We set $f_c = 1\%$ to represent ELG-like catastrophics, corresponding to the contamination rate in eBOSS and DESI galaxies. As discussed in section 2.3, to mimic redshift errors expected in slitless surveys, we consider a scenario combining LRG-like Gaussian smearing ($\sigma_{\Delta v} = 85.7\,\mathrm{km}\cdot\mathrm{s}^{-1}$) with $f_c = 5\%$ ELG-like catastrophics. The contaminated mocks are summarized in Table 1 and the distributions of ELG-like catastrophics and sliltless-like errors are shown in the right panel of Figure 1.

4 Methods

4.1 Power spectrum estimator

We estimate the power spectrum of mock catalogs using the weighted galaxy density field with a convenient normalization [44]:

$$F(\mathbf{r}) = \frac{w(\mathbf{r})\,[n_g(\mathbf{r}) - \alpha n_s(\mathbf{r})]}{A_g^{1/2}} \tag{4.1}$$

where $w(\mathbf{r})$ is the weight function. n_g and n_s are the observed number densities of galaxy and random catalogs, respectively. The factor $\alpha = N_g/N_s$ normalizes the contribution from the random, and the normalization factor A is defined with the expected mean space density of galaxies $\bar{n}(\mathbf{r})$ as $A_g = \int d\mathbf{r}\,[\bar{n}(\mathbf{r})w(\mathbf{r})]^2$. The estimator of power spectrum multipoles P_ℓ is given by [44, 45]:

$$P_\ell(k) = (2\ell+1)\int \frac{d\Omega_k}{4\pi}\left[\int d\mathbf{r}_1 \int d\mathbf{r}_2 F(\mathbf{r}_1)F(\mathbf{r}_2) \times e^{i\,\mathbf{k}\cdot(\mathbf{r}_1-\mathbf{r}_2)}\mathcal{L}_\ell(\hat{\mathbf{k}}\cdot\hat{\mathbf{r}}_h) - \mathrm{SN}_\ell\right] \tag{4.2}$$

Here, $\mathcal{L}_\ell$ is the Legendre polynomial and $\mathbf{r}_h = (\mathbf{r}_1 + \mathbf{r}_2)/2$. The shot noise term SN_ℓ is expressed as $\mathrm{SN}_\ell(\mathbf{k}) = (1+\alpha)\int d\mathbf{r}\,\bar{n}(\mathbf{r})w^2(\mathbf{r})\mathcal{L}_\ell(\hat{\mathbf{k}}\cdot\hat{\mathbf{r}})$, which only contributes to monopole ($\ell = 0$) and is negligible relative to P_ℓ for $\ell > 0$. In practice, we use the `pypower`[1] [45] to compute the power spectrum multipoles from our mock catalogs.

4.2 Galaxy clustering models

4.2.1 Effective-field theory of LSS

Effective field theory (`EFT`) has become a powerful tool to model the LSS of the Universe. By studying small-scale nonlinear physics, the `EFT` of LSS extends the standard perturbation theory to scales beyond the breakdown of the fluid and single-stream approximations [46–48]. With loop corrections and improved modeling of biased tracers with redshift-space distortions, `EFT` enables reliable predictions of the galaxy power spectrum multipoles up to

[1] https://github.com/cosmodesi/pypower

$k \approx 0.25\,h\,\mathrm{Mpc}^{-1}$ in redshift space [49–53]. In general, the galaxy redshift-space power spectrum in EFT framework is expressed as [8]:

$$P_{g,s}^{\mathtt{EFT}}(k,\mu) = P_{g,s}^{\mathrm{PT}}(k,\mu) + (\alpha_0 + \alpha_2\mu^2 + \alpha_4\mu^4 + ...)k^2 P_{g,s}^{\mathrm{L}}(k) + \left(\mathrm{SN}_0 + \mathrm{SN}_2 \mathrm{k}^2\mu^2 + ...\right), \quad (4.3)$$

Here, μ is the cosine of the angle between the wavenumber vector $\mathbf{k}$ and light-of-sight. $P_{g,s}^{\mathrm{PT}}$ is the galaxy redshift-space power spectrum based on perturbation theory (Standard, Euclidian or Lagrangian...). It is derived from the linear matter power spectrum, incorporating loop corrections and galaxy bias parameters, such as b_1, b_2 and b_s. The second terms are the general EFT counterterms parameterized by α_i, which models the non-perturbative physics and the nonlinear mapping between real and redshift space. The last term corresponds to the stochastic contributions characterized by the shot noise parameters $\mathrm{SN_i}$. The EFT of LSS approach has been successfully applied in recent analyses of BOSS, eBOSS and DESI, leading to direct constraints on cosmological parameters using the full-shape of power spectrum [7, 9]. Several EFT codes are publicly available [54–56], and have demonstrated consistent performance in the full-shape analysis [57]. In our work, we use the FOLPSν^2 [56] code to calculate the EFT power spectrum.

4.2.2 Full-Shape fitting approaches

We adopt two fitting strategies to perform full-shape cosmological inference: ShapeFit compression [58] and Full-Modeling. These approaches have been extensively tested and validated in analyses of the BOSS and DESI surveys [8, 59–62].

Compression analysis focuses on fitting a set of compressed physical parameters that describe the shape and the anisotropies of the galaxy power spectrum. These include the scaling parameters $\alpha_\parallel$, $\alpha_\perp$ and the growth rate $f\sigma_8$. The scaling parameters are often reparameterized into the isotropic dilation parameter $\alpha_{\mathrm{iso}} \equiv \alpha_\parallel^{1/3}\alpha_\perp^{2/3}$ and the Alcock-Paczynski (AP) parameter $\alpha_{\mathrm{ap}} \equiv \alpha_\parallel \alpha_\perp^{-1}$. ShapeFit further introduces two shape-related parameters, m and n, to capture information from the early-time transfer function. In this work, we vary only one shape parameter m, while keeping n fixed [8, 58]. We report ShapeFit results relative to a reference cosmology, specifically using $dm \equiv m - 1$ and $df \equiv f/f^{\mathrm{fid}}$.

Another fitting approach, known as Full-Modeling analysis, avoids the compression steps and directly fits cosmological models to the power spectrum signals. In this way, the parameter dependence of the linear power spectrum along and geometrical information are not kept separate. This allows for a direct comparison between theoretical predictions and observational data and thus gives direct constraints on parameters. In our baseline fitting procedure, we consider five cosmological parameters: h, ω_{cdm}, ω_b, $\ln(10^{10}A_s)$, n_s. These parameters are directly used in theoretical models, which facilitates the calculation and a direct comparison of cosmological biases introduced by redshift errors.

In the context of redshift error studies, ShapeFit provides a direct view of how redshift errors distort the shape of observed power spectrum, as reflected by their impact on compressed physical parameters. This makes the interpretation of redshift errors effect straightforward. The Full-Modeling approach, on the other hand, gives cosmological constraints, allowing us to quantify the biases introduced by redshift errors in final cosmological constraints.

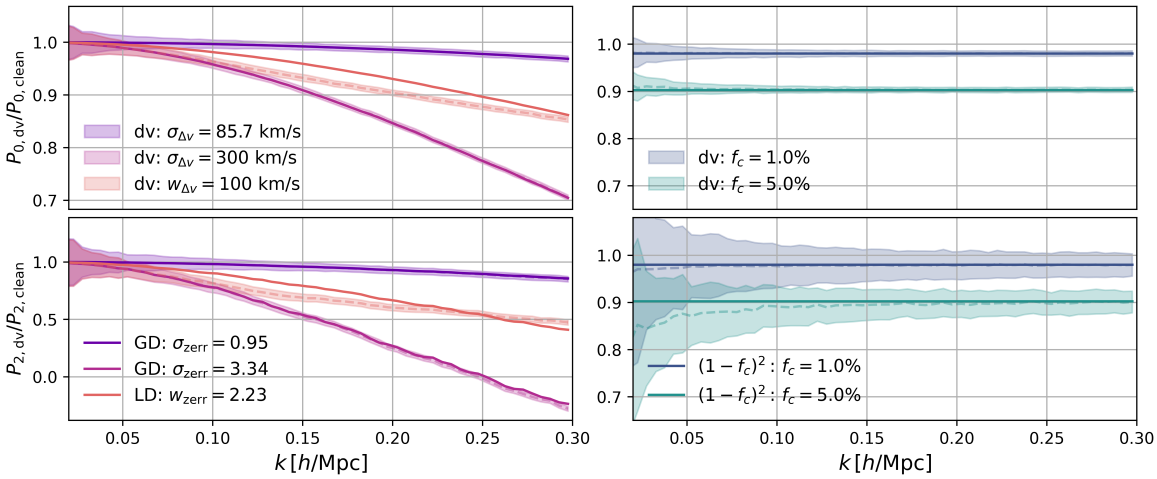

Figure 2: Power spectrum monopole and quadrupole ratios from the mean of 500 mocks (dashed line) compare to theoretical model (solid lines). The shaded regions correspond to the errors from the standard deviation of the 500 mocks divided by 5. *Left*: Comparison between the ratios from mocks contaminated by Gaussian or Lorentzian smearing (characterized by $\sigma_{\Delta v}$ and $\mathrm{w}_{\Delta v}$ respectively) relative to clean mocks with the Gaussian Damping (GD) or Lorentzian Damping (LD) factor. *Right*: Comparison between $f_c = 1\%$ and 5% contamination mock ratios with the $(1 - f_c)^2$ scaling.

4.3 Clustering effect of redshift errors

4.3.1 Redshift uncertainty damping

As pointed out in the eBOSS QSO analyses [20, 24], an approach to model the impact of redshift uncertainty in power spectrum is to introduce an additional damping term $D(k, \mu)$:

$$P_{g,s}^{\mathrm{smear}}(k, \mu) = P_{g,s}(k, \mu)\, D(k, \mu) \tag{4.4}$$

$$D(k, \mu) = \begin{cases} \exp\left[-(k\mu\sigma_{\mathrm{zerr}})^2\right], & \text{Gaussian damping,} \\ 1/\left[1 + (k\mu \mathrm{w}_{\mathrm{zerr}})^2\right], & \text{Lorentzian damping.} \end{cases} \tag{4.5}$$

where the redshift error parameters σ_{zerr} or $\mathrm{w}_{\mathrm{zerr}}$ quantify the scale of redshift uncertainty. For the Gaussian smearing case, σ_{zerr} is related to the smearing value with $\sigma_{\mathrm{zerr}} = \sigma_{\Delta v} * (1 + z)/H(z)$, and, as shown in the left panels of Figure 2, this smearing effects are well captured by the Gaussian damping factor up to $k \sim 0.3\, h\,\mathrm{Mpc}^{-1}$. In the Lorentzian smearing case, the parametrization implies an additional factor of two, i.e. $\mathrm{w}_{\mathrm{zerr}} = 2\,\mathrm{w}_{\Delta v} * (1 + z)/H(z)$. With Lorentzian damping, we see deviations compared to our mock analyses (orange lines in Figure 2). This is possibly due to the velocity cut we applied when constructing the Lorentzian smearing profile. However, as we will demonstrate in the following, these deviations can be effectively absorbed within the more flexible `EFT` framework.

To compare the damping factor with `EFT` model, we can apply the Taylor expansion on the damping terms. For both Gaussian and Lorentzian smearing, we have:

$$D(k, \mu) \to 1 + a_2(k\mu)^2 + a_4(k\mu)^4 + \ldots \tag{4.6}$$

[2] https://github.com/henoriega/FOLPS-nu

We notice that the second and third terms scale as $P(k)(k\mu)^2$ and $P(k)(k\mu)^4$, respectively. These terms have similar structures to those of EFT counterterms in Eq. (4.3). In the EFT of LSS, the general form of such counterterms can be derived from a moment expansion of the redshift-space power spectrum [50, 53, 63], as well as from comparisons with phenomenological models [6]. Consistently, [64] has shown that the leading corrections coming from redshift uncertainty are degenerate with EFT counterterms, particularly those parameterized by α_2 and α_4. In section 5.2.1, we demonstrate equivalently that the redshift uncertainty effect can be absorbed by the EFT nuisance parameters. Therefore, when we do the cosmological fitting, we use the EFT-based clustering model without including the additional damping factor.

4.3.2 Redshift catastrophics correction

Redshift catastrophics have been addressed in theoretical models for redshift surveys like WiggleZ [14] and more recently *Euclid* [23]. Assuming that the redshift catastrophic contamination rate is f_c, an approximate correction is to multiply the EFT galaxy power spectrum by a factor of $(1-f_c)^2$:

$$P_{g,s}^{\mathtt{EFT}+f_c}(k,\mu) \approx (1-f_c)^2 P_{g,s}^{\mathtt{EFT}}(k,\mu) \tag{4.7}$$

The validity of this approximation depends both on f_c and the displacement caused by catastrophics. In Figure 2, based on our mock analyses with contamination $f_c = 1\%$ and 5%, we find that the relative difference between the correction factor, $R_{\rm corr} \equiv (1-f_c)^2$, and the ratio from the mock statistics, $R_{\rm mock} \equiv P_{{\rm dv},\,f_c}/P_{\rm clean}$, satisfies:

$$\left|\frac{R_{\rm corr}(k) - R_{\rm mock}(k)}{R_{\rm mock}(k)}\right| \lesssim 6\%, \quad \text{For } 0.02 \leq \mathrm{k} \leq 0.3\,\mathrm{h\,Mpc}^{-1} \tag{4.8}$$

This suggests that the approximation is sufficiently accurate for full-shape power spectrum analysis, especially considering that additional nuisance parameters in the EFT can absorb residual mismatches. In DESI, the f_c is typically below 1%. Their overall impact is expected to be small [21] and such correction is not included in the standard EFT model. However, in slitless surveys such as *Euclid*, where f_c is significantly higher, we will show in section 5.2.2 that incorporating this correction will be necessary to obtain unbiased cosmological constraints.

4.4 Cosmological inference and Covariance matrices

Cosmological inference employs Bayesian statistics to infer constraints on physical or cosmological parameters. Assuming the evidence from the data is normalized to one, the posterior probability is expressed as $P(\Theta|\mathcal{D}) \propto \mathcal{L}(\mathcal{D}|\Theta)P(\Theta)$, with Θ being the set of input parameters, including compressed parameters $\{\alpha_{\rm iso},\ \alpha_{\rm ap},\ df,\ dm\}$ by ShapeFit or cosmological parameters $\{h,\ \omega_{cdm},\ \omega_b,\ \ln(10^{10}\mathrm{A_s}),\ \mathrm{n_s}\}$ by Full-Modeling. It also contains nuisance parameters considered in the EFT model: $\{b_1,\ b_2,\ b_s,\ \alpha_0,\ \alpha_2,\ \alpha_4,\ \mathrm{SN}_0,\ \mathrm{SN}_2\}$. Assuming that we have Gaussian-distributed data, the likelihood function can be expressed as $\mathcal{L}(\Theta) \propto e^{-\chi^2(\Theta)/2}$. The χ^2 statistic quantifies the goodness of fitting and is computed based on the difference between the observed data and the model predictions, which reads as:

$$\chi^2(\Theta) = \left(\mathcal{D}_{\rm data} - \mathcal{D}_{\rm model}(\Theta)\right)^T \mathcal{C}^{-1} \left(\mathcal{D}_{\rm data} - \mathcal{D}_{\rm model}(\Theta)\right) \tag{4.9}$$

In our study, the vector $\mathcal{D}$ includes a combination of the power spectrum monopole $P_0(k)$ and quadrupole $P_2(k)$. The subscript 'data' and 'model' refers to the measurements from

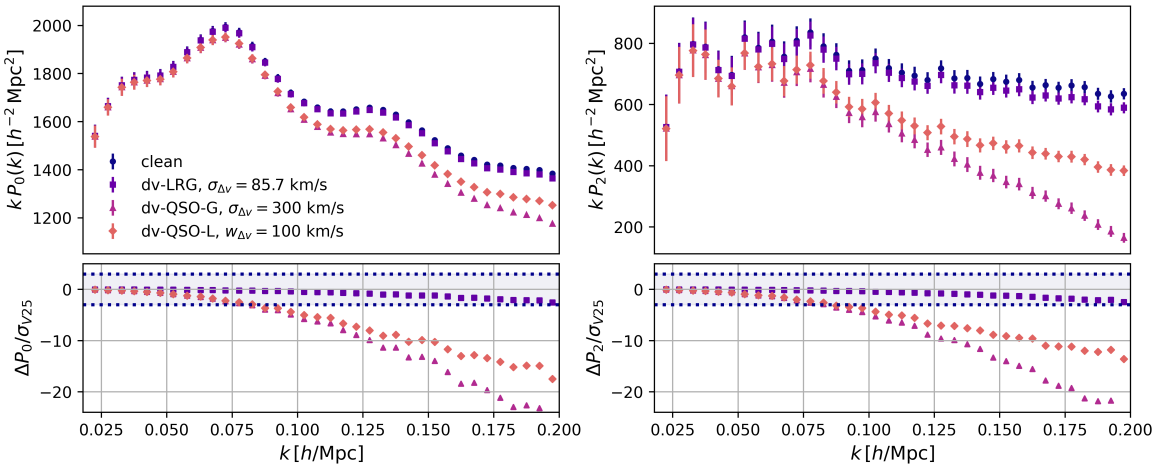

Figure 3: Comparison of power spectrum monopole (left) and quadrupole (right) between clean mocks and mocks contaminated by redshift uncertainties. The error bars, σ, are rescaled to match an effective survey volume of V_{25}. The lower panels show their residuals in units of clean mocks σ, with the dotted line indicating the 3σ threshold. In QSO-like Gaussian or Lorentzian smearing cases, we see significant deviations ($> 3\sigma$) for $k \gtrsim 0.09\,h\,\mathrm{Mpc}^{-1}$.

observations (here mocks) and theoretical model predictions. For each type of redshift-error, we have constructed 500 corresponding contaminated mocks and use them to build the data vector and covariance matrix. The covariance matrix $\mathcal{C}$ is computed and normalized to the number of the datasets, N_d, with the formulation:

$$\mathcal{C}_{ij} = \frac{1}{N_d - 1} \sum_{n=1}^{N_d} \left(\mathcal{D}_i^{(n)} - \overline{\mathcal{D}}_i\right)\left(\mathcal{D}_j^{(n)} - \overline{\mathcal{D}}_j\right), \tag{4.10}$$

The $\mathcal{D}_i^{(n)}$ denotes the i-th bin of the data vector from the n-th mock realization and $\overline{\mathcal{D}}_i$ is the ensemble mean. In QUIJOTE suite, the volume of each realization is $V_1 = 1\,h^{-3}\mathrm{Gpc}^3$. To model the reduced cosmic variance expected from galaxy surveys, we use the rescaled covariance as: $\mathcal{C}' = (V_1/V_n)\,\mathcal{C}$, where V_n is the target survey volume. In our analyses, we rescale the covariance to an effective volume of $V_{25} = 25\,h^{-3}\mathrm{Gpc}^3$ to match the expected survey volumes of DESI and *Euclid*.

5 Results

5.1 Impact of redshift errors on clustering statistics

The impact of redshift errors on the clustering statistics is presented in Figure 3 and Figure 4. For redshift uncertainty, it introduces a smearing effect that systematically suppresses the power spectrum amplitude, with the suppression becoming stronger at smaller scales (i.e., larger k). The lower panels of Figure 3 show the residual plot in units of the clean mocks error bar σ. For an effective survey volume of V_{25}, the LRG-like smearing leads to minimal impacts on the clustering, with power spectrum difference $\Delta P < 3\sigma$. For QSO-like redshift uncertainty, both Lorentzian and Gaussian smearing lead to $\Delta P > 3\sigma$ for $k \gtrsim 0.09\,h\,\mathrm{Mpc}^{-1}$ in the monopole and quadrupole. Notably, the QSO Lorentzian smearing, with the same RMS value as the Gaussian case, shows a comparatively flatter suppression at large k.

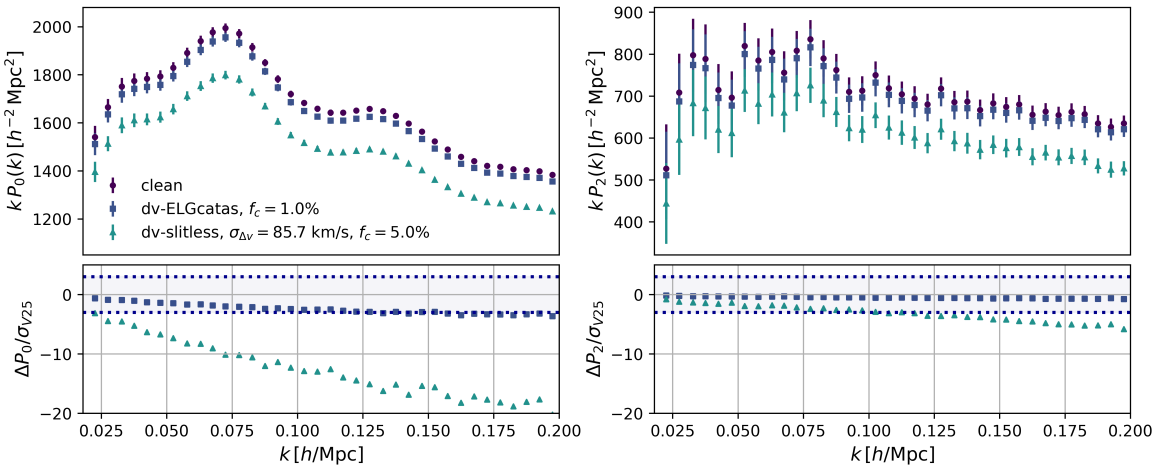

Figure 4: Similar to Figure 3 comparing clean mocks and mocks contaminated by ELG-like catastrophics and slitless-like errors. Redshift catastrophics introduce an overall suppression on power spectrum amplitude, leading $> 3\sigma$ difference for sliltess-like errors.

Redshift catastrophics affect only a small fraction of objects but cause significant shifts on their positions along the line-of-sight. Section 4.3.2 shows that this distortion leads to an overall reduction on the power spectrum, scaling approximately as $(1 - f_c)^2$. As illustrated in Figure 4, the ELG-like catastrophics with $f_c = 1\%$ leads to a 2% reduction of the clustering amplitude, with maximum deviations around 3σ. However, slitless-like errors (i.e., $\sigma_v = 85.7\,\mathrm{km}\cdot\mathrm{s}^{-1}$ and $f_c = 5\%$) introduce an overall suppression of the power spectrum amplitude by 10%-12%, resulting in a deviation $> 3\sigma$ for $k \gtrsim 0.02\,h\,\mathrm{Mpc}^{-1}$ in the monopole and $k \gtrsim 0.12\,h\,\mathrm{Mpc}^{-1}$ in the quadrupole. Such 3σ deviations, if uncorrected, could bias cosmological inferences. In the following subsections, we will describe their impact when running the inference in different cosmological cases: ΛCDM, w_0w_aCDM and massive neutrino.

5.2 Baseline Fitting

Our baseline full-shape analysis fits the power spectrum monopole and quadrupole over the range $0.02 \leq k \leq 0.2\,h\,\mathrm{Mpc}^{-1}$, using the standard `EFT` model without including the damping term from redshift uncertainty or the correction factor from redshift catastrophics. We adopt two fitting strategies, ShapeFit and Full-Modeling, to extract cosmological information. The results are presented within the standard flat-ΛCDM model assuming a BBN prior on baryon abundance Ω_b and wide Gaussian prior on spectral index n_s. The cosmological inference is performed using the `desilike`[3] package and parameter priors are set to the same as the those in DESI DR1 full-shape analysis [8]. The parameter space is sampled with the code `emcee` [65]. All plots and confidence intervals are generated using the `GetDist` package [66]. Beside the baseline full-shape analysis, we also evaluate the impact of redshift errors on BAO fitting. These results are discussed in section A.

5.2.1 Cosmological influence

In this section, we assess the impact of redshift errors on cosmological inference. These results are based on 200 independent fits to the Quijote mocks catalogs in Table 1. For each fit, we

[3] https://github.com/cosmodesi/desilike

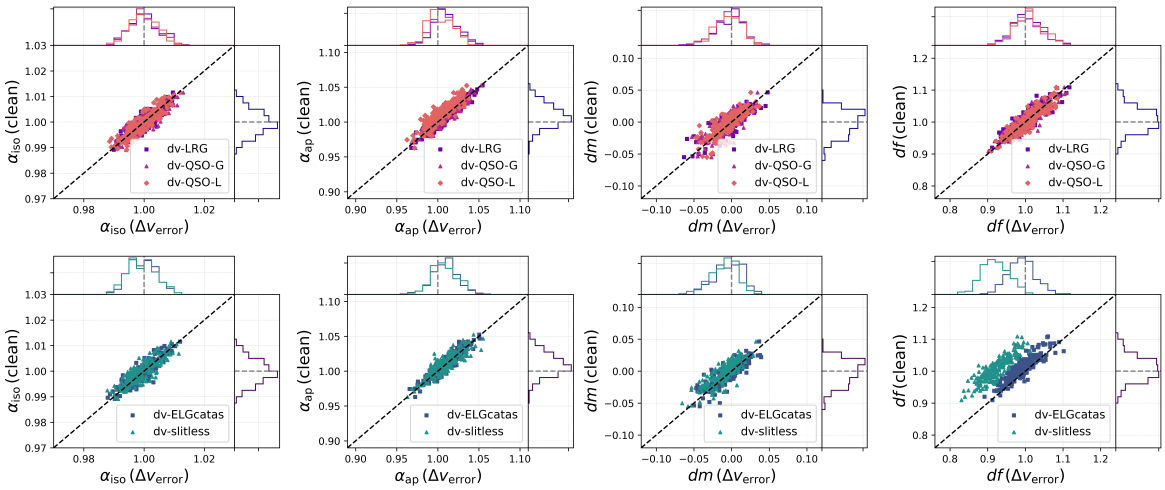

Figure 5: Distributions of the best-fit values for ShapeFit compressed parameters. Scatter plots compare results from clean and contaminated mocks in Table 1. Each point represents one fit to the mean of 25 random mocks, with the covariance rescaled to volume V_{25}. The corresponding marginalized histograms are shown in the right and top subpanels. The parameter estimates remain consistent across most cases, except for df, which shows a notable deviation in mocks contaminated by slitless-like errors.

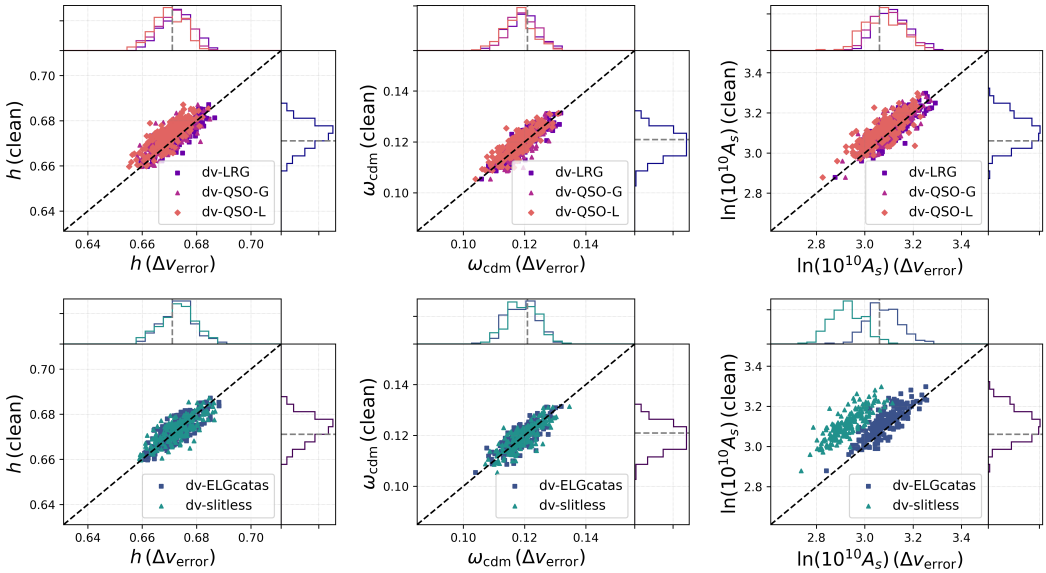

Figure 6: Same plots as Figure 5 for Full-Modeling cosmological parameters. As before, results from clean and contaminated mocks in Table 1 are compared. Only $\ln(10^{10}A_s)$ shows a notable deviation in mocks contaminated by slitless-like errors.

use the mean power spectrum derived from 25 randomly selected mocks (drawn from 500), with a covariance matrix rescaled to the volume V_{25}. Comparisons of the best-fit parameters between analyses from clean and contaminated mocks are presented in Figure 5 for ShapeFit and in Figure 6 for Full-Modeling. The corresponding χ^2 comparison, provided in section B,

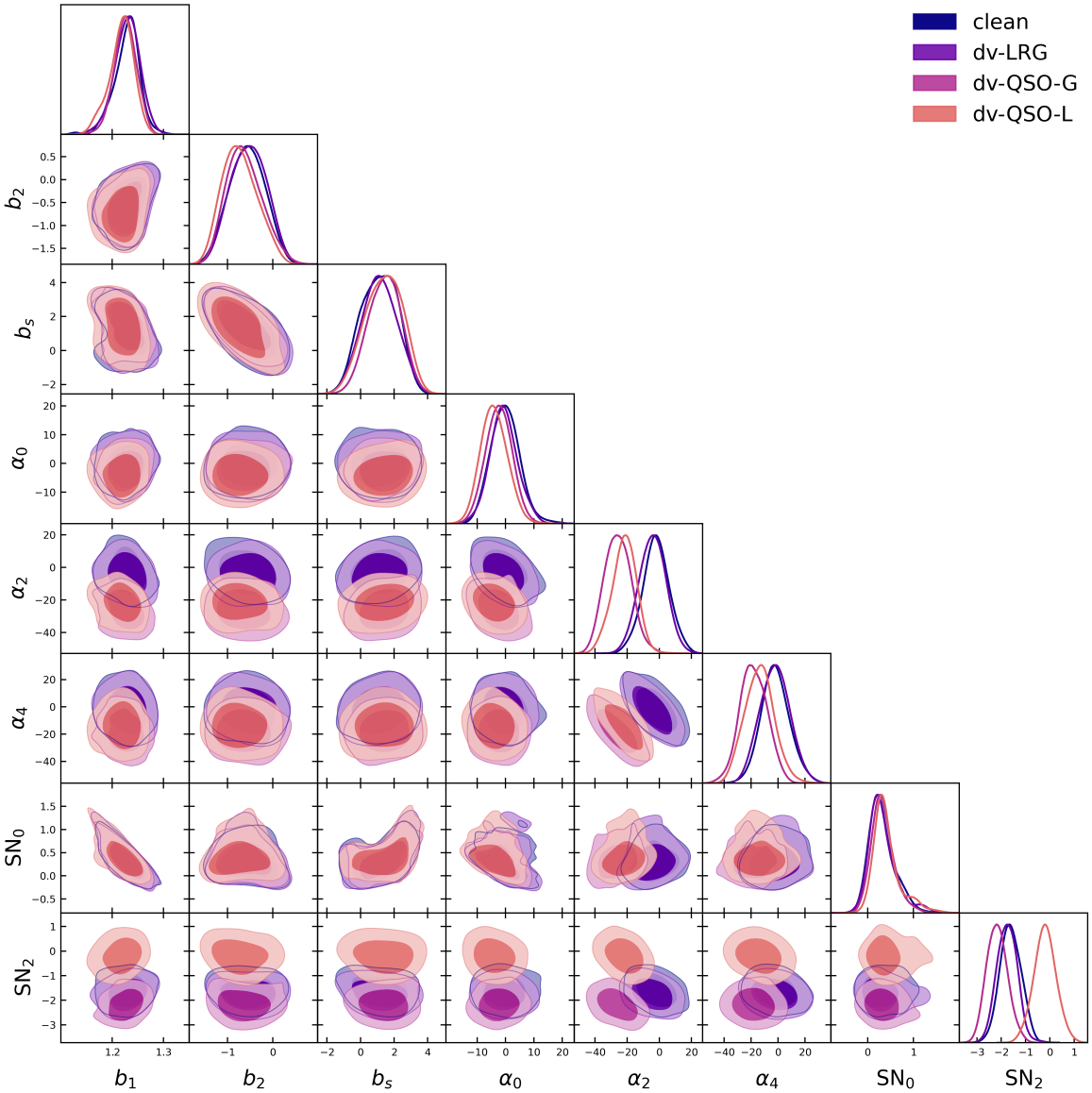

Figure 7: Posterior distribution for nuisance parameters in our baseline EFT fitting. Constraints are compared from clean mocks (dark blue) and those contaminated by redshift uncertainties: LRG-like Gaussian (purple), QSO-like Gaussian (pink) and QSO-like Lorentzian (red) smearings. Contours show the 68% and 95% confidence level. Results are derived from fits to the mean power spectrum monopole and quadrupole of 25 mocks using covariance rescaled to V_{25}. The marginalized posteriors of α_2 and α_4 show negative shifts, reflecting the smearing effect of redshift uncertainty, while the positive shift of SN_2 shows the difference brought by the Lorentzian smearing.

confirms that all our fits achieved comparable goodness-of-fit.

In Figure 5 and Figure 6, the upper panels illustrate the impact of redshift uncertainty on cosmological inference. The fitting results from both ShapeFit and Full-Modelling indicate that no significant bias (<5%) in cosmological parameter estimates. As discussed in

Theory	EFT baseline			EFT + free f_c	EFT + fixed f_c
Mocks	clean	dv-ELGcatas	dv-slitless	dv-slitless	dv-slitless
$\ln(10^{10}A_s)$	3.125 ± 0.084	3.095 ± 0.081	2.941 ± 0.085	3.13 ± 0.14	3.042 ± 0.079

Table 2: Constraints on $\ln(10^{10}A_s)$ for clean and contaminated mocks fitted by different theoretical models. Table shows the mean values with 68% confidence intervals. In EFT baseline fit, the mean values from ELG-like catastrophics and sliltless-like errors show deviations of 0.4σ and 2.2σ, respectively, compared to the clean case. By multiplying the factor $(1-f_c)^2$ to the galaxy power spectrum, the extended model f_c, EFT + free f_c recovers an unbiased value of $\ln(10^{10}A_s)$ but increases its error bar by 67% due to parameter degeneracies. Fixing the f_c to its expected value, the EFT + fixed f_c model restores the constraining power with a modest bias of 1.0σ.

section 4.3.1, the suppression of the power spectrum caused by redshift uncertainty is expected to be absorbed by EFT counterterms. Figure 7 plots the posterior distributions of all nuisance parameters. These posteriors reveal negative shifts in α_2 and α_4, consistent with the expected absorption of the damping effect. Another parameter that shows variation is SN_2, which represents the second-order stochastic term and scales as $(k\mu)^2$. Its positive shift in the Lorentzian smearing case could be led by the flatter suppression pattern of the Lorentzian profile at large k.

The lower panels of Figure 5 and Figure 6 assess the impact of redshift catastrophics and hypothetical slitless-like errors on cosmological inference. The ELG-like catastrophics with $f_c = 1\%$ show negligible bias in parameter estimates (with the largest discrepancy $< 6\%$), consistent with the previous findings in [21]. In contrast, slitless-like errors with $f_c = 5\%$ show noticeable biases, particularly in estimating the fractional growth rate parameter df in ShapeFit and the log primordial amplitude parameter $\ln(10^{10}A_s)$ in Full-Modeling. Both parameters are systematically underestimated by $6\%-16\%$ compared to clean case. We identify that this negative shift arises mainly from the 5% catastrophic contamination in slitless-like errors, which significantly suppresses the power spectrum amplitude (see Figure 3). If not adequately modeled in theory, this effect could bias the estimates of amplitude-related parameters. Nevertheless, in section 4.3.2, an approximate correction by multiplying the power spectrum by a factor of $(1 - f_c)^2$ can mitigate this suppression. In the following section, we incorporate this correction into the cosmological analyses to further investigate the influence of redshift catastrophics.

5.2.2 Catastrophics-correction for slitless survey

In this test, we present Full-Modeling fitting results based on the mean power spectrum calculated from all 500 mocks, with the covariance matrix rescaled to volume V_{25}. By averaging over 500 mocks, we minimize the impact of cosmic variance, so any observed deviations in parameter estimates can be more confidently attributed to redshift errors. The left panel of Figure 8 shows the posterior distributions of parameters using the baseline EFT fit for three contamination cases: clean, ELG-like catastrophics ($f_c = 1\%$), and slitless-like errors (i.e., $\sigma_v = 85.7\mathrm{km} \cdot \mathrm{s}^{-1}$ and $f_c = 5\%$). The corresponding mean values of $\ln(10^{10}A_s)$ with 68% confidence intervals are summarized in Table 2. Comparing the $\ln(10^{10}A_s)$ constraint from clean case, we find a small shift of 0.4σ by ELG-like catastrophics and a significant one of 2.2σ

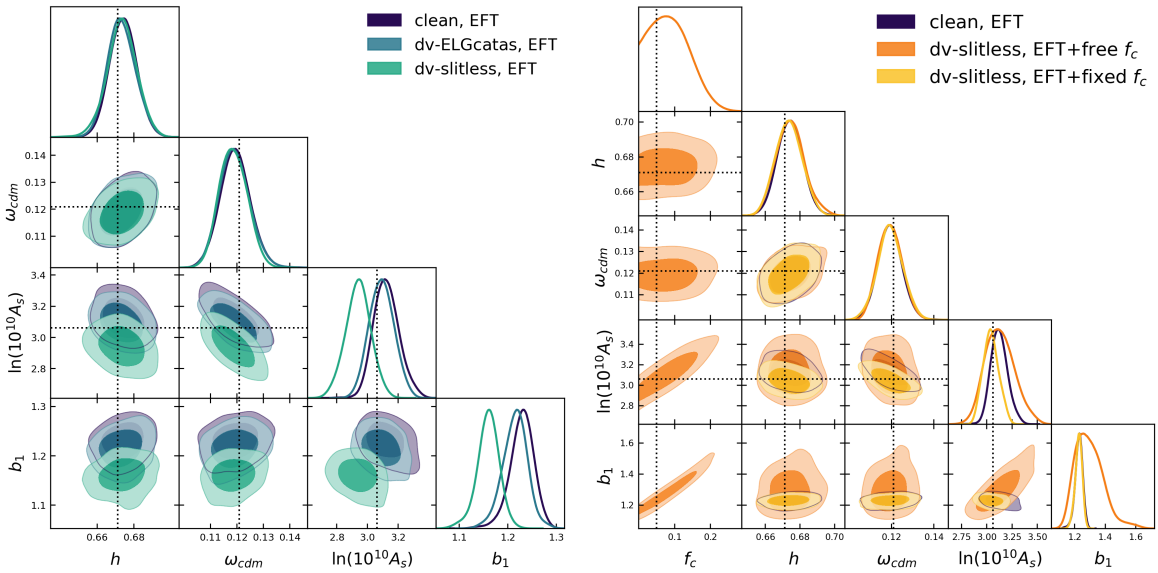

Figure 8: Posterior distributions for Full-Modeling parameters. *Left panel*: Constraints using the baseline EFT model to fit clean mocks (dark blue), mocks contaminated by ELG-like catastrophics ($f_c = 1\%$; blue), and slitless-like errors ($\sigma_v = 85.7\text{km} \cdot \text{s}^{-1}$ with $f_c = 5\%$; green). *Right panel*: Comparison between clean results with slitless-like errors using the extended EFT model when freeing f_c (EFT + free f_c; orange) and with f_c fixed to its expected value (EFT + fixed f_c; yellow). Contours show 68% and 95% confidence intervals with black dash lines indicating the true values. Results are derived from fits to the mean power spectrum monopole and quadrupole of 500 mocks using the covariance matrix rescaled to V_{25}. The marginalized posteriors of $\ln(10^{10}A_s)$ and b_1 are shifted by slitless-like errors, but using the corrected model with f_c help restore the estimated values.

by slitless-like errors. These results are consistent with our earlier findings in section 5.2.1. The linear bias parameter b_1 is also known to be related to the overall amplitude of galaxy power spectrum. In Figure 8, we find a shift of 2.7σ in its mean value for the slitless-like errors case using baseline EFT. We note that b_1 is highly degenerate with f_c and $\ln(10^{10}A_s)$, but the shift in b_1 is insufficient to compensate for the bias induced by slitless-like errors on $\ln(10^{10}A_s)$.

To incorporate the effect of catastrophics in the clustering model, we extend the baseline EFT model by adding an additional parameter, catastrophic rate f_c, and multiplying the factor $(1 - f_c)^2$ to the galaxy power spectrum as described in Eq. (4.7). When freeing f_c parameter during sampling with a flat prior $f_c \in [0, 1]$, we refer to the EFT + free f_c model. The posterior distributions, including the variation of f_c, are shown in the right panel of Figure 8, with the corresponding constraint on $\ln(10^{10}A_s)$ reported in Table 2. The EFT + free f_c model succeed in recovering an unbiased mean value of $\ln(10^{10}A_s)$ for slitless-like errors, with a discrepancy below 0.1σ compared to the clean case. However, this improvement comes at the cost of loss in constraining power: we measure a $\sim 67\%$ degradation in the $\ln(10^{10}A_s)$ constraint. This loss is due to the strong degeneracy between f_c and $\ln(10^{10}A_s)$, as illustrated in the Figure 8 $\ln(10^{10}A_s) - f_c$ plane. When fixing the parameter f_c to its expected value, referred to the EFT + fixed f_c model, we successfully recover the constraining power but find a slightly larger deviation ($\sim 1.0\sigma$) in the estimated mean value. This deviation is possibly due to

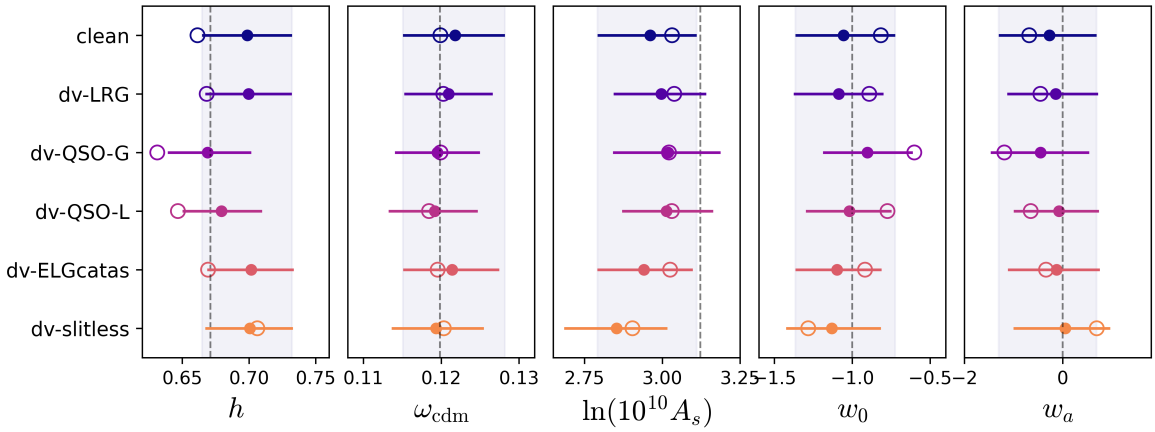

Figure 9: Parameter constraints on w_0w_aCDM model for clean and contaminated mocks. The horizontal error bars indicate mean and the 68% credible levels of the corresponding posterior. The shaded region show the 1σ constraints from the clean mocks. While redshift errors do not introduce bias in the measurement of dark energy properties w_0, w_a, they potentially lead to stronger projection effects, which are deviations between the MAP values (open circles) with the mean of the posterior, particularly with QSO-like smearing.

the combined effects of redshift uncertainty in the slitless-like errors and the approximation applied in the correction model.

This test is informative for slitless spectroscopy survey like *Euclid*, which aims to constrain cosmological parameters via galaxy power spectra. As we have shown that this hypothetical redshift errors can bias cosmological inference, an accurate estimation of the catastrophics rate and the implementation of the catastrophics-corrected model, either with f_c fixed or varied under a narrow Gaussian prior, are necessary to get unbiased constraints. Since our slitless-like errors scenario is optimistic and slitless survey may have other additional complex systematics, further investigations on modeling redshift errors are still required.

5.3 Beyond ΛCDM cosmologies

Recent spectroscopic surveys such as DESI have extended full-shape power spectrum analysis beyond the standard ΛCDM framework to test cosmological models with evolving dark energy (w_0w_aCDM) and massive neutrinos. Assuming a flat Universe and combining the full-shape and BAO analyses with external datasets, the DESI DR2 finds a mild preference for a dynamical dark energy model with $w_0 > -1$ and $w_a < 0$ [5] and places a tight constraint on the total neutrino mass, $\sum m_\nu < 0.0642\,\mathrm{eV}$ (95%CL) [67]. This section investigates how redshift errors affect the measurements of dark energy equation of state w_0-w_a and $\sum m_\nu$ through the full-shape analysis. In the following, we use the baseline `EFT` fitting setup and present results obtained by fitting the mean power spectrum of 500 mocks, with the covariance matrix rescaled to the effective volume V_{25}.

5.3.1 Evolving dark energy

We assess the influence of redshift errors on the measurement of evolving dark energy using the Chevallier-Polarski-Linder (CPL) parametrization $w(a) = w_0 + w_a(1-a)$ [68, 69]. The cosmological fits are performed using the QUIJOTE fiducial mocks described in section 3, which

Catalogs	clean	dv-LRG	dv-QSO-G	dv-QSO-L	dv-ELGcatas	dv-slitless
$\sum m_\nu$	$< 0.78\,\mathrm{eV}$	$< 0.69\,\mathrm{eV}$	$< 1.40\,\mathrm{eV}$	$< 0.94\,\mathrm{eV}$	$< 0.84\,\mathrm{eV}$	$< 0.85\,\mathrm{eV}$

Table 3: Comparison of 95% confidence upper bounds on the sum of neutrino masses, $\sum m_\nu$. Results are obtained using Full-Modeling analysis with $\sum m_\nu$ varied and fitting power spectrum monopole and quadrupole of 500 mocks with covariance rescaled to V_{25}. Both clean and contaminated mock catalogs are considered with $\sum m_\nu = 0.1\,\mathrm{eV}$. We find that redshift uncertainties degrade the neutrino mass constraint up to $\sim 80\%$ in QSO-like smearing cases, whereas ELG-like redshift catastrophics and slitless-like errors show negligible effect.

assume a ΛCDM model with $w_0 = -1$ and $w_a = 0$. The resulting parameter constraints are shown as the horizontal lines in Figure 9. From the comparisons, we find that redshift errors do not introduce significant bias in the measurement of dark energy properties. However, we know that using full-shape analysis alone to constraint $w_0 w_a$CDM model suffer from projection effects [8]. To study this aspect, we use `iminuit` [70] to estimate the maximum a *posteriori* (MAP) value, starting from the maximum log-posterior points found in MCMC chains. In Figure 9, we find offsets between the mean of the marginalised posteriors (solid circles) and MAP values (open circles) for parameters h, w_0 and w_a, with the offsets being most pronounced for mocks contaminated by QSO-like smearing. Since the redshift errors impact the clustering pattern similarly with the behavior of certain parameters (cosmological or nuisance), their presence could complicate the parameter degeneracies and thus amplify projection effects. Such impact should be investigated in more detail for redshift surveys aiming to constrain dark energy by full-shape analysis.

5.3.2 Massive neutrinos

For the massive neutrino case, we use the QUIJOTE Mnu_p catalogs with $\sum m_\nu = 0.1\,\mathrm{eV}$ to build our clean and contaminated mock catalogs. During the fitting, we allow $\sum m_\nu$ to vary with a flat prior of $\mathcal{U}(0.0, 5.0)\,\mathrm{eV}$ in the ΛCDM framework. The upper limits of $\sum m_\nu$ at 95% confidence level for all mocks analyses are presented in Table 3. We first note that using full-shape analysis alone to constrain the $\sum m_\nu$ has slow convergence and large uncertainties, particularly for the low neutrino mass case. Nevertheless, we find that redshift uncertainty introduces extended tails in the $\sum m_\nu$ posterior distribution, leading to a weaker constraint on the neutrino mass. Compared to the clean case ($< 0.78\,\mathrm{eV}$), the 95% upper limits increase by up to $\sim 80\%$ when QSO Gaussian smearing is included. This degradation occurs because both massive neutrinos and redshift uncertainty have similar suppression on small-scale power spectrum. Massive neutrinos do so through their thermal velocities and free-streaming, while redshift uncertainty smears the clustering structure along the line of sight. This degeneracy complicates the convergence and leads to weaker constraints on neutrino mass. In contrast, we find no noticeable bias in the $\sum m_\nu$ measurements due to ELG-like catastrophic failures or slitles-like redshift errors.

6 Conclusions

In this paper, we investigate the impact of spectroscopic redshift errors on cosmological measurements. section 2 introduces the redshift errors, which can affect redshift measurements

in both ground-based (fiber-fed) and space-based (slitless) spectroscopic surveys [17, 21, 35]. There are two main types of redshift errors. Redshift uncertainty refer to small errors present in all redshift measurements, and redshift catastrophic failures correspond to large deviations from the true values in a small fraction of the measurements. Both type of errors distort the observed clustering pattern and can lead to biases in the inferred cosmological results.

The effect of redshift errors can be quantified and modeled using repeat observations. In section 3 we use the QUIJOTE simulation suite to construct our contaminated mock catalogs. For redshift uncertainty, we consider Gaussian or Lorentzian profiles for LRG-like and QSO-like smearing [19, 26]. For redshift catastrophics, we use a log-normal distribution [21] with contamination rate $f_c = 1\%$ to model ELG-like catastrophics. The slitless-like errors assume a hypothetical scenario combining $f_c = 5\%$ catastrophics and LRG-like uncertainty to simulate the observing condition in slitless survey. The following section 4 describes the methodologies to perform the full-shape power spectrum analysis. In our baseline fitting, we use clustering models based on the effective field theory (`EFT`) of LSS, without including the damping term or the multiplicative factor. We implement both ShapeFit and Full-Modeling fitting approach to extract cosmological information. The analysis is targeted on DESI- and *Euclid*-like surveys with effective volume $V_{25} = 25\,h^{-3}\mathrm{Gpc}^3$. Our key findings are summarized below:

Redshift uncertainty introduces diffusive effect in the clustering, leading to a scale-dependent suppression to the observed power spectrum. The `EFT` counterterms, parameterized by α_2 and α_4, capture this smearing effect, resulting in compressed and cosmological parameter estimates difference $< 5\%$ compared to the uncontaminated case. In contrast, redshift catastrophics cause an overall reduction on the power spectrum amplitude that approximately scales as $(1 - f_c)^2$. While this effect is negligible (difference $< 6\%$) for ELG-like catastrophics, it significantly biases the estimation of amplitude-related parameters for slitless-like errors, namely df in ShapeFit and $\ln(10^{10}A_s)$ in the Full-Modeling. In that case, we observe shifts of $6\%-16\%$, corresponding to a $\sim 2.2\sigma$ deviation relative to the clean case. To model this effect, we use the correction factor $(1 - f_c)^2$ applied to the power spectrum in Eq. (4.7). When freeing f_c, the extended model mitigates the bias in $\ln(10^{10}A_s)$ to below 0.1σ, but leads to 67% degradation in its precision due to the strong degeneracy between f_c and $\ln(10^{10}A_s)$. Fixing f_c to its expected value in the fit restores the constraining power with a modest 1.0σ deviation. This highlights the importance of accurately estimating the catastrophic failure rate f_c and applying the appropriate correction model to ensure unbiased cosmological results in slitless spectroscopic surveys.

Beyond the vanilla ΛCDM model, we explore the impact of redshift errors on the measurement of evolving dark energy and massive neutrinos. For the w_0w_aCDM model, we find that redshift errors do not bias the estimates of w_0 and w_a, although they can potentially enhance projection effects. In the massive neutrino case, redshift errors weaken the constraint on $\sum m_\nu$ up to 80% when considering QSO-like Gaussian smearing.

For future work, we plan to apply our framework to the DESI DR2 analysis. The DESI DR2 dataset provides a large sample of repeat observations well-suited for characterizing redshift errors. Using this dataset, we aim to jointly model redshift uncertainty and catastrophic failures for each tracer population across a wide range of redshift. We also plan to conduct more detailed investigations of redshift errors, including lightcone effects, redshift evolution, impact on all various clustering statistics and so on.

Acknowledgments

SH, AR, JY and JPK, acknowledge support from the Swiss National Science Foundation (SNF) 'Cosmology with 3D Maps of the Universe" research grant 200020_207379. This research was essentially supported by computational resources provided by the High Performance Computing (HPC) facility of University of Geneva (UNIGE), especially for the Bamboo cluster.

References

[1] D.J. Eisenstein and W. Hu, *Baryonic Features in the Matter Transfer Function*, *The Astrophysical Journal* **496** (1998) 605.

[2] D.J. Eisenstein, I. Zehavi, D.W. Hogg, R. Scoccimarro, M.R. Blanton, R.C. Nichol et al., *Detection of the Baryon Acoustic Peak in the Large-Scale Correlation Function of SDSS Luminous Red Galaxies*, *The Astrophysical Journal* **633** (2005) 560.

[3] D.H. Weinberg, M.J. Mortonson, D.J. Eisenstein, C. Hirata, A.G. Riess and E. Rozo, *Observational probes of cosmic acceleration*, *Physics Reports* **530** (2013) 87.

[4] S. Alam, M. Ata, S. Bailey, F. Beutler, D. Bizyaev, J.A. Blazek et al., *The clustering of galaxies in the completed SDSS-III Baryon Oscillation Spectroscopic Survey: cosmological analysis of the DR12 galaxy sample*, *Monthly Notices of the Royal Astronomical Society* **470** (2017) 2617.

[5] DESI Collaboration, M. Abdul-Karim, J. Aguilar, S. Ahlen, S. Alam, L. Allen et al., *DESI DR2 Results II: Measurements of Baryon Acoustic Oscillations and Cosmological Constraints*, *Physical Review D* **112** (2025) 083515.

[6] M.M. Ivanov, M. Simonović and M. Zaldarriaga, *Cosmological Parameters from the BOSS Galaxy Power Spectrum*, *Journal of Cosmology and Astroparticle Physics* **2020** (2020) 042.

[7] G. D'Amico, J. Gleyzes, N. Kokron, D. Markovic, L. Senatore, P. Zhang et al., *The Cosmological Analysis of the SDSS/BOSS data from the Effective Field Theory of Large-Scale Structure*, *Journal of Cosmology and Astroparticle Physics* **2020** (2020) 005.

[8] DESI Collaboration, A.G. Adame, J. Aguilar, S. Ahlen, S. Alam, D.M. Alexander et al., *DESI 2024 V: Full-Shape Galaxy Clustering from Galaxies and Quasars*, (2025), 10.48550/arXiv.2411.12021.

[9] DESI Collaboration, A.G. Adame, J. Aguilar, S. Ahlen, S. Alam, D.M. Alexander et al., *DESI 2024 VII: Cosmological Constraints from the Full-Shape Modeling of Clustering Measurements*, *Journal of Cosmology and Astroparticle Physics* **2025** (2025) 028.

[10] DESI Collaboration, A. Aghamousa, J. Aguilar, S. Ahlen, S. Alam, L.E. Allen et al., *The DESI Experiment Part I: Science,Targeting, and Survey Design*, (2016), 10.48550/arXiv.1611.00036.

[11] DESI Collaboration, A. Aghamousa, J. Aguilar, S. Ahlen, S. Alam, L.E. Allen et al., *The DESI Experiment Part II: Instrument Design*, (2016), 10.48550/arXiv.1611.00037.

[12] R. Laureijs, J. Amiaux, S. Arduini, J.-L. Auguères, J. Brinchmann, R. Cole et al., *Euclid Definition Study Report*, (2011), 10.48550/arXiv.1110.3193.

[13] Euclid Collaboration, Y. Mellier, Abdurro'uf, J.A.A. Barroso, A. Achúcarro, J. Adamek et al., *Euclid. I. Overview of the Euclid mission*, *Astronomy & Astrophysics* **697** (2025) A1.

[14] C. Blake, S. Brough, M. Colless, W. Couch, S. Croom, T. Davis et al., *The WiggleZ Dark Energy Survey: the selection function and z=0.6 galaxy power spectrum*, *Monthly Notices of the Royal Astronomical Society* (2010) no.

[15] A.S. Bolton, D.J. Schlegel, E. Aubourg, S. Bailey, V. Bhardwaj, J.R. Brownstein et al., *Spectral Classification and Redshift Measurement for the SDSS-III Baryon Oscillation Spectroscopic Survey*, *The Astronomical Journal* **144** (2012) 144.

[16] J. Guy, S. Bailey, A. Kremin, S. Alam, D.M. Alexander, C.A. Prieto et al., *The Spectroscopic Data Processing Pipeline for the Dark Energy Spectroscopic Instrument*, *The Astronomical Journal* **165** (2023) 144.

[17] Euclid Collaboration, V.L. Brun, M. Bethermin, M. Moresco, D. Vibert, D. Vergani et al., *Euclid Quick Data Release (Q1) – Characteristics and limitations of the spectroscopic measurements*, (2025), 10.48550/arXiv.2503.15308.

[18] C. Blake, T. Davis, G. Poole, D. Parkinson, S. Brough, M. Colless et al., *The WiggleZ Dark Energy Survey: testing the cosmological model with baryon acoustic oscillations at z=0.6*, *Monthly Notices of the Royal Astronomical Society* **415** (2011) 2892.

[19] P. Zarrouk, E. Burtin, H. Gil-Marin, A.J. Ross, R. Tojeiro, I. Paris et al., *The clustering of the SDSS-IV extended Baryon Oscillation Spectroscopic Survey DR14 quasar sample: measurement of the growth rate of structure from the anisotropic correlation function between redshift 0.8 and 2.2*, *Monthly Notices of the Royal Astronomical Society* **477** (2018) 1639.

[20] J. Hou, A.G. Sánchez, A.J. Ross, A. Smith, R. Neveux, J. Bautista et al., *The Completed SDSS-IV extended Baryon Oscillation Spectroscopic Survey: BAO and RSD measurements from anisotropic clustering analysis of the Quasar Sample in configuration space between redshift 0.8 and 2.2*, *Monthly Notices of the Royal Astronomical Society* **500** (2020) 1201.

[21] J. Yu, A.J. Ross, A. Rocher, O. Alves, A.d. Mattia, D. Forero-Sánchez et al., *ELG Spectroscopic Systematics Analysis of the DESI Data Release 1*, *Journal of Cosmology and Astroparticle Physics* **2025** (2025) 126.

[22] A. Krolewski, J. Yu, A.J. Ross, S. Penmetsa, W.J. Percival, R. Zhou et al., *Impact and mitigation of spectroscopic systematics on DESI DR1 clustering measurements*, (2025), 10.48550/arXiv.2405.17208.

[23] Euclid Collaboration, I. Risso, A. Veropalumbo, E. Branchini, E. Maragliano, S.d.l. Torre et al., *Euclid preparation. The impact of redshift interlopers on the two-point correlation function analysis*, (2025), 10.48550/arXiv.2505.04688.

[24] A. Smith, E. Burtin, J. Hou, R. Neveux, A.J. Ross, S. Alam et al., *The Completed SDSS-IV Extended Baryon Oscillation Spectroscopic Survey: N-body Mock Challenge for the Quasar Sample*, *Monthly Notices of the Royal Astronomical Society* **499** (2020) 269.

[25] J. Yu, C. Zhao, C.-H. Chuang, J. Bautista, G. Favole, J.-P. Kneib et al., *Model BOSS & eBOSS Luminous Red Galaxies at $0.2 < z < 1.0$ using SubHalo Abundance Matching with 3 parameters*, *Monthly Notices of the Royal Astronomical Society* **516** (2022) 57.

[26] J. Yu, C. Zhao, V. Gonzalez-Perez, C.-H. Chuang, A. Brodzeller, A.d. Mattia et al., *The DESI One-Percent Survey: Exploring A Generalized SHAM for Multiple Tracers with the UNIT Simulation*, (2023), 10.48550/arXiv.2306.06313.

[27] DESI Collaboration, M. Abdul-Karim, A.G. Adame, D. Aguado, J. Aguilar, S. Ahlen et al., *Data Release 1 of the Dark Energy Spectroscopic Instrument*, (2025), 10.48550/arXiv.2503.14745.

[28] Euclid Collaboration, G. Polenta, M. Frailis, A. Alavi, P.N. Appleton, P. Awad et al., *Euclid Quick Data Release (Q1). NIR processing and data products*, (2025), 10.48550/arXiv.2503.15304.

[29] Euclid Collaboration, Y. Copin, M. Fumana, C. Mancini, P.N. Appleton, R. Chary et al., *Euclid Quick Data Release (Q1): From spectrograms to spectra: the SIR spectroscopic Processing Function*, (2025), 10.48550/arXiv.2503.15307.

[30] C. Hahn, M.J. Wilson, O. Ruiz-Macias, S. Cole, D.H. Weinberg, J. Moustakas et al., *DESI Bright Galaxy Survey: Final Target Selection, Design, and Validation*, *The Astronomical Journal* **165** (2023) 253.

[31] R. Zhou, B. Dey, J.A. Newman, D.J. Eisenstein, K. Dawson, S. Bailey et al., *Target Selection and Validation of DESI Luminous Red Galaxies*, *The Astronomical Journal* **165** (2023) 58.

[32] A. Raichoor, J. Moustakas, J.A. Newman, T. Karim, S. Ahlen, S. Alam et al., *Target Selection and Validation of DESI Emission Line Galaxies*, *The Astronomical Journal* **165** (2023) 126.

[33] E. Chaussidon, C. Yèche, N. Palanque-Delabrouille, D.M. Alexander, J. Yang, S. Ahlen et al., *Target Selection and Validation of DESI Quasars*, *The Astrophysical Journal* **944** (2023) 107.

[34] Euclid Collaboration, H. Aussel, I. Tereno, M. Schirmer, G. Alguero, B. Altieri et al., *Euclid Quick Data Release (Q1) – Data release overview*, (2025), 10.48550/arXiv.2503.15302.

[35] A.J. Ross, J. Bautista, R. Tojeiro, S. Alam, S. Bailey, E. Burtin et al., *The Completed SDSS-IV extended Baryon Oscillation Spectroscopic Survey: Large-scale Structure Catalogs for Cosmological Analysis*, *Monthly Notices of the Royal Astronomical Society* **498** (2020) 2354.

[36] A. Raichoor, A.d. Mattia, A.J. Ross, C. Zhao, S. Alam, S. Avila et al., *The completed SDSS-IV extended Baryon Oscillation Spectroscopic Survey: Large-scale Structure Catalogues and Measurement of the isotropic BAO between redshift 0.6 and 1.1 for the Emission Line Galaxy Sample*, *Monthly Notices of the Royal Astronomical Society* **500** (2020) 3254.

[37] B.W. Lyke, A.N. Higley, J.N. McLane, D.P. Schurhammer, A.D. Myers, A.J. Ross et al., *The Sloan Digital Sky Survey Quasar Catalog: Sixteenth Data Release*, *The Astrophysical Journal Supplement Series* **250** (2020) 8.

[38] T.-W. Lan, R. Tojeiro, E. Armengaud, J.X. Prochaska, T.M. Davis, D.M. Alexander et al., *The DESI Survey Validation: Results from Visual Inspection of Bright Galaxies, Luminous Red Galaxies, and Emission Line Galaxies*, *The Astrophysical Journal* **943** (2023) 68.

[39] D.M. Alexander, T.M. Davis, E. Chaussidon, V.A. Fawcett, A.X. Gonzalez-Morales, T.-W. Lan et al., *The DESI Survey Validation: Results from Visual Inspection of the Quasar Survey Spectra*, *The Astronomical Journal* **165** (2023) 124.

[40] D. Spergel, N. Gehrels, C. Baltay, D. Bennett, J. Breckinridge, M. Donahue et al., *Wide-Field InfrarRed Survey Telescope-Astrophysics Focused Telescope Assets WFIRST-AFTA 2015 Report*, (2015), 10.48550/arXiv.1503.03757.

[41] CSST Collaboration, Y. Gong, H. Miao, H. Zhan, Z.-Y. Li, J. Shangguan et al., *Introduction to the China Space Station Telescope (CSST)*, (2025), 10.48550/arXiv.2507.04618.

[42] F. Villaescusa-Navarro, C. Hahn, E. Massara, A. Banerjee, A.M. Delgado, D.K. Ramanah et al., *The Quijote simulations*, *The Astrophysical Journal Supplement Series* **250** (2020) 2.

[43] Planck Collaboration, N. Aghanim, Y. Akrami, M. Ashdown, J. Aumont, C. Baccigalupi et al., *Planck 2018 results. VI. Cosmological parameters*, *Astronomy & Astrophysics* **641** (2020) A6.

[44] H.A. Feldman, N. Kaiser and J.A. Peacock, *Power Spectrum Analysis of Three-Dimensional Redshift Surveys*, *The Astrophysical Journal* **426** (1994) 23.

[45] N. Hand, Y. Li, Z. Slepian and U. Seljak, *An optimal FFT-based anisotropic power spectrum estimator*, *Journal of Cosmology and Astroparticle Physics* **2017** (2017) 002.

[46] D. Baumann, A. Nicolis, L. Senatore and M. Zaldarriaga, *Cosmological Non-Linearities as an Effective Fluid*, *Journal of Cosmology and Astroparticle Physics* **2012** (2012) 051.

[47] J.J.M. Carrasco, M.P. Hertzberg and L. Senatore, *The Effective Field Theory of Cosmological Large Scale Structures*, *Journal of High Energy Physics* **2012** (2012) 82.

[48] Z. Vlah, M. White and A. Aviles, *A Lagrangian effective field theory*, *Journal of Cosmology and Astroparticle Physics* **2015** (2015) 014.

[49] P. McDonald and A. Roy, *Clustering of dark matter tracers: generalizing bias for the coming era of precision LSS*, *Journal of Cosmology and Astroparticle Physics* **2009** (2009) 020.

[50] L. Senatore and M. Zaldarriaga, *Redshift Space Distortions in the Effective Field Theory of Large Scale Structures*, (2014), 10.48550/arXiv.1409.1225.

[51] L. Senatore, *Bias in the Effective Field Theory of Large Scale Structures*, *Journal of Cosmology and Astroparticle Physics* **2015** (2015) 007.

[52] S.-F. Chen, Z. Vlah, E. Castorina and M. White, *Redshift-Space Distortions in Lagrangian Perturbation Theory*, *Journal of Cosmology and Astroparticle Physics* **2021** (2021) 100.

[53] A. Aviles, G. Valogiannis, M.A. Rodriguez-Meza, J.L. Cervantes-Cota, B. Li and R. Bean, *Redshift space power spectrum beyond Einstein-de Sitter kernels*, *Journal of Cosmology and Astroparticle Physics* **2021** (2021) 039.

[54] S.-F. Chen, Z. Vlah and M. White, *Consistent Modeling of Velocity Statistics and Redshift-Space Distortions in One-Loop Perturbation Theory*, *Journal of Cosmology and Astroparticle Physics* **2020** (2020) 062.

[55] G. D'Amico, L. Senatore and P. Zhang, *Limits on wCDM from the EFTofLSS with the PyBird code*, *Journal of Cosmology and Astroparticle Physics* **2021** (2021) 006.

[56] H.E. Noriega, A. Aviles, S. Fromenteau and M. Vargas-Magaña, *Fast computation of non-linear power spectrum in cosmologies with massive neutrinos*, *Journal of Cosmology and Astroparticle Physics* **2022** (2022) 038.

[57] M. Maus, Y. Lai, H.E. Noriega, S. Ramirez-Solano, A. Aviles, S. Chen et al., *A comparison of effective field theory models of redshift space galaxy power spectra for DESI 2024 and future surveys*, (2024), 10.48550/arXiv.2404.07272.

[58] S. Brieden, H. Gil-Marín and L. Verde, *ShapeFit: extracting the power spectrum shape information in galaxy surveys beyond BAO and RSD*, *Journal of Cosmology and Astroparticle Physics* **2021** (2021) 054.

[59] M. Maus, S.-F. Chen and M. White, *A comparison of template vs. direct model fitting for redshift-space distortions in BOSS*, *Journal of Cosmology and Astroparticle Physics* **2023** (2023) 005.

[60] H.E. Noriega, A. Aviles, H. Gil-Marín, S. Ramirez-Solano, S. Fromenteau, M. Vargas-Magaña et al., *Comparing Compressed and Full-modeling Analyses with FOLPS: Implications for DESI 2024 and beyond*, (2024), 10.48550/arXiv.2404.07269.

[61] M. Maus, S. Chen, M. White, J. Aguilar, S. Ahlen, A. Aviles et al., *An analysis of parameter compression and full-modeling techniques with Velocileptors for DESI 2024 and beyond*, (2024), 10.48550/arXiv.2404.07312.

[62] Y. Lai, C. Howlett, M. Maus, H. Gil-Marín, H.E. Noriega, S. Ramírez-Solano et al., *A comparison between Shapefit compression and Full-Modelling method with PyBird for DESI 2024 and beyond*, (2024), 10.48550/arXiv.2404.07283.

[63] G. D'Amico, L. Senatore, P. Zhang and T. Nishimichi, *Taming redshift-space distortion effects in the EFTofLSS and its application to data*, *Journal of Cosmology and Astroparticle Physics* **2024** (2024) 037.

[64] T. Simon, P. Zhang and V. Poulin, *Cosmological inference from the EFTofLSS: the eBOSS QSO full-shape analysis*, *Journal of Cosmology and Astroparticle Physics* **2023** (2023) 041.

[65] D. Foreman-Mackey, D.W. Hogg, D. Lang and J. Goodman, *emcee: The MCMC Hammer*, *Publications of the Astronomical Society of the Pacific* **125** (2013) 306.

[66] A. Lewis, *GetDist: a Python package for analysing Monte Carlo samples*, (2025), 10.48550/arXiv.1910.13970.

[67] W. Elbers, A. Aviles, H.E. Noriega, D. Chebat, A. Menegas, C.S. Frenk et al., *Constraints on Neutrino Physics from DESI DR2 BAO and DR1 Full Shape*, (2025), 10.48550/arXiv.2503.14744.

[68] M. Chevallier and D. Polarski, *Accelerating Universes with Scaling Dark Matter*, *International Journal of Modern Physics D* **10** (2001) 213.

[69] E.V. Linder, *Exploring the Expansion History of the Universe*, *Physical Review Letters* **90** (2003) 091301.

[70] F. James and M. Roos, *Minuit - a system for function minimization and analysis of the parameter errors and correlations*, *Computer Physics Communications* **10** (1975) 343.

[71] DESI Collaboration, A.G. Adame, J. Aguilar, S. Ahlen, S. Alam, D.M. Alexander et al., *DESI 2024 III: Baryon Acoustic Oscillations from Galaxies and Quasars*, *Journal of Cosmology and Astroparticle Physics* **2025** (2025) 012.

A BAO fitting results

Catalogs	clean	dv-LRG	dv-QSO-G	dv-QSO-L	dv-ELGcatas	dv-slitless
$\alpha_{\rm iso}$	1.003 ± 0.005	1.003 ± 0.005	1.002 ± 0.005	1.003 ± 0.004	1.003 ± 0.005	1.003 ± 0.005
$\alpha_{\rm ap}$	1.002 ± 0.016	0.998 ± 0.016	0.998 ± 0.016	0.999 ± 0.017	1.000 ± 0.017	0.998 ± 0.017
$\chi^2/\rm dof$	1.102 ± 0.274	1.090 ± 0.250	1.109 ± 0.259	1.064 ± 0.229	1.074 ± 0.222	1.061 ± 0.230

Table 4: Comparison of BAO best-fit results for the clean and contaminated mock catalogs described in Table 1. Table reports the mean and standard deviation of best-fit values from 200 fits. The $\alpha_{\rm iso}$ and $\alpha_{\rm ap}$ constraints remain unbiased in the presence of redshift errors. The corresponding best-fit χ^2 over the degree of freedom (dof) shows the same level of goodness-of-fit.

BAO serves as a standard ruler in cosmology and is generally considered robust against a wide range of systematic effects. In this work, we also test whether BAO measurements remain unbiased under the spectroscopic redshift errors. BAO analysis focuses on constraining two dilation parameters, $\alpha_\parallel$ and $\alpha_\perp$, which are reparameterized into two scaling parameters, $\alpha_{\rm iso}$ and $\alpha_{\rm ap}$, respectively. These two parameters provide information about the isotropic BAO scale and AP effect. We adopt the BAO modeling framework implemented in DESI DR1 analysis [71] using the `desilike` package. The results are obtained by fitting the monopole and quadrupole of the two-point correlation function from the mean of 25 randomly selected mocks out of 500 realizations without BAO reconstruction. The covariance matrix is built from 500 mocks and rescaled to an effective volume of $V_{25} = 25\,h^{-3}{\rm Gpc}^3$.

Table 4 summarizes the mean and standard deviation for $\alpha_{\rm iso}$ and $\alpha_{\rm ap}$ best-fit values and χ^2 obtained from 200 independent fits. The inferred $\alpha_{\rm iso}$ and $\alpha_{\rm ap}$ values show only minor differences from the clean case, both in their means and standard deviations. The best-fit χ^2 values also show no increase after including redshift errors, indicating a same level of goodness of fit. Therefore, we conclude that BAO measurements remain unbiased and robust against spectroscopic redshift errors at the current level of precision.

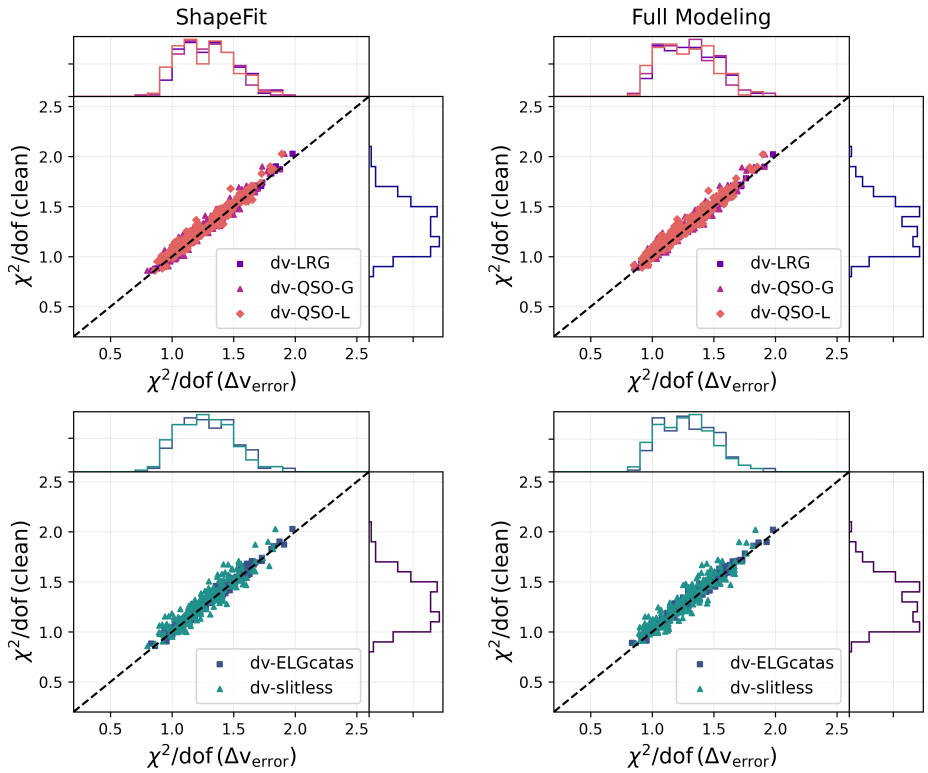

Figure 10: Comparison of corresponding χ^2 for Figure 5 and Figure 6. The best-fit χ^2 values are normalized by the degrees of freedom, with results for ShapeFit (left panels) and Full Modeling (right panels). For each point, we fit the mean of 25 random mocks, with the covariance rescaled to V_{25}. The difference of χ^2 is small between clean and contaminated mock catalogs, demonstrating that all fits achieve the same level of goodness.

B χ^2 results for baseline analysis

Figure 10 presents the distribution of best-fit χ^2 values for the baseline analysis. The left two panels show results for the ShapeFit analysis, corresponding to the scatter plot in Figure 5, while the right two panels show the Full-Modeling results for Figure 6. From the χ^2 distributions, we do not observe significant differences ($<$15%) or systematic shifts between the clean and contaminated mocks analyses. This indicates that the theoretical model provides a same level of good prediction with the observational data, even potential deviations in the parameter estimates may arise under contamination.